

Multiphoton ionization of the Calcium atom by linearly and circularly polarized laser fields

Gabriela Buica

*Institute for Space Sciences, P.O. Box MG-23,
Ro 77125, Bucharest-Măgurele, Romania*

Takashi Nakajima*

*Institute of Advanced Energy, Kyoto University,
Gokasho, Uji, Kyoto 611-0011, Japan*

Abstract

We theoretically study multiphoton ionization of the Ca atom irradiated by the second (photon energy 3.1 eV) and third (photon energy 4.65 eV) harmonics of Ti:sapphire laser pulses (photon energy 1.55 eV). Because of the dense energy level structure the second and third harmonics of a Ti:sapphire laser are nearly single-photon resonant with the $4s4p\ ^1P^o$ and $4s5p\ ^1P^o$ states, respectively. Although two-photon ionization takes place through the near-resonant intermediate states with the same symmetry in both cases, it turns out that there are significant differences between them. The photoelectron energy spectra exhibit the absence/presence of substructures. More interestingly, the photoelectron angular distributions clearly show that the main contribution to the ionization processes by the third harmonic arises from the far off-resonant $4s4p\ ^1P^o$ state rather than the near-resonant $4s5p\ ^1P^o$ state. These findings can be attributed to the fact that the dipole moment for the $4s^2\ ^1S^e - 4s5p\ ^1P^o$ transition is much smaller than that for the $4s^2\ ^1S^e - 4s4p\ ^1P^o$ transition.

PACS numbers: 32.80.Rm, 42.50.Hz

Keywords:

*t-nakajima@iae.kyoto-u.ac.jp

I. INTRODUCTION

Above-threshold ionization (ATI) [1] is a process in which atoms absorb more than the minimum number of photons required to ionize and the photoelectron energy spectrum (PES) consists of a series of peaks that are equally separated by the photon energy. Now the ATI and multiphoton ionization (MPI) processes have been well-studied [2, 3], especially for rare gas atoms. Recently, we have presented several new interesting features in the PES of a light alkaline-earth-metal atom, Mg, interacting with a short laser pulse [4, 5]. We have had a close look at *the intermediate ATI peaks* appearing in the PES and clarified their origin as the *off-resonant* excitation of the bound states. In this paper we extend our previous works on Mg to another alkaline-earth-metal atom which is less investigated in the literature, the Ca atom.

During the last 30 years many theoretical and experimental investigations have been performed for Ca to obtain the atomic data and to understand its interaction with laser fields for the *single-photon processes*. The first extensive theoretical studies for the singlet series 1S and 1P of Ca were performed by Fischer and Hansen [6] with a multi-configuration Hartree-Fock (MCFH) method which included correlations between the valence electrons. Later on, Mitroy [7] calculated the energy level and oscillator strength (OS) for the low-lying levels of Ca using the frozen-core Hartree-Fock (FCHF) approach including a model potential. Aymar and co-workers [8] extensively studied light alkaline-earth-metal atoms using the multichannel quantum defect theory and eigenchannel R-matrix combined with polarization potentials. Hansen and co-workers [9] used a configuration interaction (CI) approach, based on the B-spline basis functions and a model potential with dielectronic core polarization potential, to calculate term energies and wave functions for the singlet and triplet states of Ca. Recently, Fischer and Tachiev [10] calculated the energy levels, transition probabilities, and lifetimes for the singlet and triplet spectra of Ca using the MCFH method with lowest-order relativistic effects included through a Breit-Pauli Hamiltonian.

As for the *MPI processes* Benec'h and Bachau [11] calculated the one-, two-, and three-photon ionization cross sections of Ca from the ground state with B-spline basis functions and CI procedure, where the FCHF approach and polarization potentials were employed to construct the atomic basis. Regarding the experimental MPI processes of Ca, there are only several works in the literature, all of which involve only ns and ps laser pulses. DiMauro and

co-workers [12] investigated single and double ionization of Ca by 10 ns Nd:YAG laser pulses at 532 and 1064 nm in the intensity range of $10^{10} - 10^{13} \text{ W/cm}^2$. Shao and co-workers [13] analyzed single and double ionization of Ca by 35 and 200 ps Nd:YAG laser pulses at 532 and 1064 nm in the intensity range of $10^{10} - 2 \times 10^{13} \text{ W/cm}^2$. Lately, Cohen and co-workers [14] experimentally and theoretically studied the two-photon ionization spectra of Ca in the 374-323 nm wavelength range with a ~ 5 ns dye laser. Although theoretical data for MPI of alkaline-earth-metal atoms such as Ca by fs laser pulses would provide additional valuable information for the purpose of understanding the multiphoton ionization dynamics, such data are still missing in the literature.

The aim of this work is to extend our previous investigations for MPI of Mg [4, 5, 15, 16] to the Ca atom: In this paper we study the MPI processes of Ca by the second (photon energy 3.1 eV) and third (photon energy 4.65 eV) harmonics of Ti:sapphire laser pulses. For this purpose we use a nonperturbative method to solve the time-dependent Schrödinger equation (TDSE) with two active electrons. In Sec. II we construct an atomic basis set in terms of discretized states and use it in Sec. III to numerically solve the TDSE. Numerical results such as the ionization yields, PES, and photoelectron angular distribution (PAD) are presented in Sec. IV. Atomic units (a.u.) are used throughout this paper unless otherwise mentioned.

II. ATOMIC BASIS STATES

The Ca atom is a two-valence-electron atom with a closed ionic core Ca^{2+} (the nucleus and the 18 inner-shell electrons $1s^2 2s^2 2p^6 3s^2 3p^6$) and the two valence electrons, $4s^2 \ ^1S^e$. Since it is a heavier alkaline-earth-metal element than Be and Mg and hence the core, Ca^{2+} , is softer, there are more complexities as well as subtleties in the Ca atomic structure. As it is already mentioned in the literature [17, 18] there are several different approaches to solve the Schrödinger equation to describe the interaction of a one- and two-valence-electron atom with a laser field. Since the general computational procedure has already been presented in Refs. [5, 16, 19–21] and the specific details about the atomic structure calculation of Ca have been reported in recent works [9, 11, 22], we only make a brief description of the method we employ. The field-free one-electron Hamiltonian of Ca^+ , $H_a(r)$, is expressed as:

$$H_a(r) = -\frac{1}{2} \frac{d^2}{dr^2} - \frac{Z}{r} + \frac{l(l+1)}{2r^2} + V_{eff}(r), \quad (1)$$

where $V_{eff}(r)$ is the effective potential acting on the valence electron of Ca^+ , r represents the position vector of the valence electron, Z is the electric charge of the core ($Z = 2$ for a two-valence-electron atom), and l is the orbital quantum number. In our approach the effective potential, $V_{eff}(r)$, consists of the FCHF potential (FCHFP) and the additional core-polarization potential which will be introduced in the next subsection.

A. One-Electron Orbitals: Frozen-Core Hartree-Fock approach

To describe the ionic core Ca^{2+} we have introduced the effective potential in Eq. (1), which is a sum of the FCHFP, $V_l^{HF}(r)$, and the core-polarization potential, $V_l^p(r, \alpha_s, r_l)$:

$$V_{eff}(r) = V_l^{HF}(r) + V_l^p(r, \alpha_s, r_l). \quad (2)$$

$V_l^p(r, \alpha_s, r_l)$ describes the interaction between the ionic core and the valence electrons and can be written in the form of

$$V_l^p(r, \alpha_s, r_l) = -\frac{\alpha_s}{2r^4} [1 - \exp^{-(r/r_l)^6}], \quad (3)$$

where α_s is the static dipole polarizability of Ca^{2+} and r_l the cutoff radii for the different orbital angular momenta, $l = 0, 1, 2, \dots$, etc [19]. The values of r_l have been obtained by performing the fittings of the one-electron energies to their experimental values [23] for the four lowest states of s , p , d and f series of Ca^+ . We have used the following set of cutoff radii, $r_0 = 1.5457$, $r_1 = 1.5857$, $r_2 = 1.8771$, and $r_{l \geq 3} = 1.5530$ together with the static dipole polarizability of Ca^{2+} which is $\alpha_s = 3.16$ [24]. The relatively large value of the cutoff radius for $l = 2$ is due to the fact the $3d$ orbital penetrates the ionic core much more than the other orbitals, and therefore the core-polarization potential is more sensitive for the $l = 2$ orbital than for other orbitals. We note that other theoretical papers [7–9, 11, 22] use slightly different values for the static dipole polarizability and cutoff radii.

With the aid of the mathematical properties of the B-spline polynomials [18, 19] to expand the one-electron orbitals, solving the one-electron Schrödinger equation for the non-relativistic one-electron Hamiltonian given by Eq. (1) is now equivalent to an eigenvalue problem.

B. Two-electron states

The field-free two-electron Hamiltonian, $H_a(\mathbf{r}_1, \mathbf{r}_2)$, can be expressed as

$$H_a(\mathbf{r}_1, \mathbf{r}_2) = \sum_{i=1}^2 H_a(r_i) + V(\mathbf{r}_1, \mathbf{r}_2), \quad (4)$$

where $H_a(r_i)$ represents the one-electron Hamiltonian for the i th electron as shown in Eq. (1), and $V(\mathbf{r}_1, \mathbf{r}_2)$ is a two-electron interaction operator which includes the static Coulomb interaction $1/|\mathbf{r}_1 - \mathbf{r}_2|$ and the effective dielectronic interaction potential [19, 25]. Here \mathbf{r}_1 and \mathbf{r}_2 are the position vectors of the two valence electrons. To solve the two-electron Schrödinger equation for the Hamiltonian given in Eq. (4) the two-electron states can be constructed within the CI approach. Namely, we use a linear combination of the products of the two one-electron orbitals to represent a two-electron states and diagonalize the two-electron Hamiltonian given in Eq.(4). This is so-called a CI procedure [19–21].

For Ca, which is heavier than Be and Mg but still relatively light alkaline-earth-metal atom, the LS coupling is known to give a fair description [7–9, 11] and hence it is sufficient to label a two-electron state by the following set of quantum numbers: principal, orbital, and spin quantum numbers for each electron, $n_i l_i s_i$ ($i = 1, 2$), total orbital momentum L , total spin S , total angular momentum J , and its projection M on the quantization axis. After the CI procedure the two-electron states may be most generally labeled by the state energy and the quantum numbers (L, S, J, M) , and furthermore the above state labeling can be simplified to (L, M) for singlet states ($S = 0$). Having obtained the two-electron wave functions we can calculate the dipole matrix elements as well as OSs for both LP and CP laser pulses.

III. TIME-DEPENDENT SCHRÖDINGER EQUATION

By making use of the two-electron states which have been constructed in Sec. II, we can solve the TDSE for the two-electron atom interacting with a laser pulse. The TDSE reads

$$i \frac{\partial}{\partial t} \Psi(\mathbf{r}_1, \mathbf{r}_2; t) = [H_a(\mathbf{r}_1, \mathbf{r}_2) + D(t)] \Psi(\mathbf{r}_1, \mathbf{r}_2; t), \quad (5)$$

where $\Psi(\mathbf{r}_1, \mathbf{r}_2; t)$ is the two-electron wave function for the two electrons located at \mathbf{r}_1 and \mathbf{r}_2 at time t , and $H_a(\mathbf{r}_1, \mathbf{r}_2)$ is the field-free two-electron Hamiltonian shown in Eq. (4). The

time-dependent interaction operator, $D(t)$, between the atom and the laser pulse is written in the velocity gauge and dipole approximation as,

$$D(t) = -\mathbf{A}(t) \cdot (\mathbf{p}_1 + \mathbf{p}_2), \quad (6)$$

where \mathbf{p}_1 and \mathbf{p}_2 are the momenta of the two electrons and $\mathbf{A}(t)$ is the vector potential of the laser field which is given by

$$\mathbf{A}(t) = \mathbf{A}_0 f(t) \cos(\omega t). \quad (7)$$

In the above equation ω is a photon energy and $\mathbf{A}_0 = A_0 \mathbf{e}_q$ is an amplitude of the vector potential with \mathbf{e}_q being the unit polarization vector of the laser pulse. The unit polarization vector is expressed in spherical coordinates, and $q = 0, 1$, and -1 correspond to the LP, right-circularly polarized, and left-circularly polarized fields, respectively. $f(t)$ represents the temporal envelope of the laser field which is assumed to be a cosine-squared function, i.e., $f(t) = \cos^2(\pi t/2\tau)$ where τ is the pulse duration for the full width at half maximum (FWHM) of the vector potential $\mathbf{A}(t)$. The temporal integration range of TDSE in Eq. (5) is taken from $-\tau$ to τ .

In order to solve Eq. (5), the time-dependent two-electron wave function, $\Psi(\mathbf{r}_1, \mathbf{r}_2; t)$, is expanded as a linear combination of two-electron states $\Psi(\mathbf{r}_1, \mathbf{r}_2; E_n)$:

$$\Psi(\mathbf{r}_1, \mathbf{r}_2; t) = \sum_{n,L,M} C_{E_n LM}(t) \Psi(\mathbf{r}_1, \mathbf{r}_2; E_n), \quad (8)$$

where $C_{E_n LM}(t)$ is a time-dependent expansion coefficient for a two-electron state with an energy, E_n , an angular momentum, L , and its projection on the quantization axis, M . Now, by substituting Eq. (8) into Eq. (5) we obtain a set of first-order differential equations for the time-dependent expansion coefficients $C_{E_n LM}(t)$ which reads

$$i \frac{d}{dt} C_{E_n LM}(t) = \sum_{n',L',M'} [E_n \delta_{nn'} \delta_{LL'} \delta_{MM'} - D_{nLMn'L'M'}(t)] C_{E_{n'} L' M'}(t), \quad (9)$$

where $D_{nLMn'L'M'}(t)$ represents the dipole matrix element between two singlet states defined by the quantum numbers (nLM) and $(n'L'M')$. This means that we have neglected the spin-forbidden transitions between the triplet and singlet states, which is a reasonably good assumption for a light atom such as Ca. Specifically in what follows, we assume that the Ca atom is initially in the ground state, $4s^2 \ ^1S^e$ ($M = 0$), i.e.,

$$|C_{E_n LM}(t = -\tau)|^2 = \delta_{n4} \delta_{L0} \delta_{M0}. \quad (10)$$

Once we have obtained the time-dependent expansion coefficients $C_{E_n LM}$ by solving Eq. (9), the ionization yield, Y , photoelectron energy spectrum, dP/dE_e , and photoelectron angular distribution, $dP/d\theta$, can be calculated at the end of the pulse from the following relations:

$$Y = 1 - \sum_{n,L,M(E_n < 0)} |C_{E_n LM}(t = +\tau)|^2, \quad (11)$$

$$\frac{dP}{dE_e}(E_e) = \sum_{L,M} |C_{E_e LM}(t = +\tau)|^2, \quad (12)$$

and

$$\frac{dP}{d\theta}(E_e, \theta) = \left| \sum_{L,M} (-i)^{l_2} e^{i\delta(E_e)} \sqrt{2l_2 + 1} P_{l_2}(\cos \theta) C_{E_e LM}(t = +\tau) \right|^2, \quad (13)$$

where E_e represents the photoelectron energy, P_{l_2} are the Legendre polynomials, l_2 is the orbital momentum of the photoelectron, and θ is the angle between the electric field and the photoelectron momentum vectors. $\delta(E_e)$ is the total phase shift which is the sum of the Coulomb and short-range scattering phase shifts. The total phase shift, $\delta(E_e)$, can be extracted from the asymptotic behavior of the photoelectron wave function [18, 19, 26, 27] at large distances $r \rightarrow \infty$:

$$\Psi_{kl_2}(r) \rightarrow \sqrt{\frac{2}{\pi k}} \sin \left[kr + \frac{1}{k} \ln(2kr) - l_2\pi/2 + \delta(E_e) \right], \quad (14)$$

where $k = (2E_e)^{1/2}$ represents the momentum of the photoelectron. Since we employ the discretized technique to describe the wave functions in a rigid spherical box, the photoelectron wave function vanishes at the edge of the box ($r = R$). This means that the following relation always holds:

$$kR + \frac{1}{k} \ln(2kR) - l_2\pi/2 + \delta(E_e) = m\pi, \quad \text{where } m \text{ is an integer}, \quad (15)$$

which enables us to calculate the total phase shift, $\delta(E_e)$.

IV. NUMERICAL RESULTS AND DISCUSSION

In this section we present representative numerical results for multiphoton ionization of Ca from the ground state by the second and third harmonics of fs Ti:sapphire laser pulses. For the numerical calculation we have found out that a spherical box of radius $R = 500$ a.u. and the total angular momentum up to $L = 9$ with 1800 states for each L gives a good convergence in terms of the ionization yield and PES. A number of 402 B -spline polynomials of order 9 with a sine-like knot grid is employed. Note that all the numerical results reported in this paper are calculated for the 20 fs (FWHM) cosine-squared pulse in the velocity gauge unless otherwise stated.

Before solving the TDSE in Eq. (5), however, we must perform several checks regarding the accuracy of the atomic basis for the singlet states of Ca. The level structure of the singlet states of Ca is presented in Fig. 1: The first ionization threshold lies at $E_{ion} = 6.11$ eV relative to the ground state. In Table I we compare our calculated energies with other theoretical results [7, 9] and the experimental data for the first ionization threshold and the first few low-lying singlet states for $L = S, P, D$, and F . The experimental data are taken from the database of National Institute of Standards and Technology (NIST) [23] and the energies are taken with respect to the double ionization threshold, Ca^{2+} . From Table I we notice that our results by the FCHF method provide energy values as accurate as other theoretical results for the ionization threshold and the first few low-lying states.

The next step is to check the accuracy of the wave function in terms of the OSs. Table II presents comparisons of the OSs for a single-photon absorption we have calculated with other theoretical [7, 9] and the experimental data [23, 28–31] for $L = S, P, D$, and F in both length and velocity gauges for the following single-photon transitions: $4s^2\ ^1S^e \rightarrow 4s(4-6)p\ ^1P^o$ and $3d4p\ ^1P^o$, $4s4p\ ^1P^o \rightarrow 4s(5-7)s\ ^1S^e$ and $4p^2\ ^1S^e$, $4s4p\ ^1P^o \rightarrow 4s(4-6)d\ ^1D^e$ and $4p^2\ ^1D^e$, $4s3d\ ^1D^e \rightarrow 4s(4-6)p\ ^1P^o$ and $3d4p\ ^1P^o$, and finally $4s3d\ ^1D^e \rightarrow 4s(4-6)f\ ^1F^o$ and $3d4p\ ^1F^o$. Clearly our results on OSs are in good agreement with other theoretical and experimental data. Relatively large discrepancies appear in the velocity gauge for the $4s3d\ ^1D^e \rightarrow 4s4p\ ^1P^o$ and $4s3d\ ^1D^e \rightarrow 3d4p\ ^1F^o$ transitions. This may be due to the insufficient accuracy of the $3d$ orbitals. Fortunately the discrepancies appear for the transitions with very small values of the OSs, and therefore could hardly influence the outcome of the TDSE calculations we report in this work.

After we have checked the accuracy of the constructed atomic basis, we can now proceed to perform the time-dependent calculations by solving Eq. (9) under various intensities and photon energies for both LP and CP laser pulses. In the following calculations we employ 1800 two-electron states for each angular momentum up to $L = 9$ and carry out the numerical integration of TDSE [Eq. (9)] using a Runge-Kutta method.

A. Ionization by the second harmonic of a Ti:sapphire laser

In this subsection we investigate two-photon ionization of Ca by the second harmonic of the Ti:sapphire laser at the photon energy $\omega = 3.1$ eV, which is schematically shown in Fig. 2. As already mentioned Ca has a relatively dense level structure and for photons in the visible range it is quite easy to be near-resonance with some bound states. Indeed, the detuning from the $4s4p\ ^1P^o$ state is only 0.17 eV, and considering the large value of the dipole matrix element for the transition $4s^2\ ^1S^e \rightarrow 4s4p\ ^1P^o$ (Table II), we expect a significant enhancement in the ionization signal.

Figure 3(a) shows the ionization yield as a function of peak intensity for LP (solid) and CP (dashed) laser pulses. The slope of these curves is about 1.85 up to the peak intensity of $I = 5 \times 10^{11}$ W/cm², after which the saturation takes place. The calculated slope is a little bit smaller than the prediction by the lowest order perturbation theory (LOPT) which gives a slope of 2 for two-photon ionization processes. Figure 3(b) shows the ratio between the ionization yield by CP and LP laser pulses, Y_{CP}/Y_{LP} , as a function of peak intensity. In the low intensity regime ($I \leq 5 \times 10^{11}$ W/cm²) the ratio slightly decreases with peak intensity and at peak intensity of 5×10^{11} W/cm² it is about 1.25, which is smaller than the ratio predicted by the perturbation theory for the two-photon ionization cross sections of one-valence-electron atoms, $\sigma_{CP}^{(2)}/\sigma_{LP}^{(2)} = 1.4$ [32–35].

In Fig. 4 we plot the PES for the LP (solid) and CP (dashed) laser pulses at the peak intensity of $I = 5 \times 10^{11}$ W/cm². The ATI peaks exhibit some small structures on the left as well on the right wings which are equidistantly separated by the photon energy. In order to clarify the importance of the near-resonant bound state $4s4p\ ^1P^o$ we solved the TDSE with the $4s4p\ ^1P^o$ state artificially removed during the numerical integration. In Fig. 5(a) we compare the PES (solid) with that calculated without the state $4s4p\ ^1P^o$ (dashed) in the atomic basis. As a consequence the ionization signal is almost 4 orders of magnitude lower

and almost all substructures on the left and right wings of the ATI peaks disappeared when $4s4p\ ^1P^o$ is removed. In order to see the population dynamics of near-resonant $4s4p\ ^1P^o$, we plot the population of $4s^2\ ^1S^e$ (circles) and $4s4p\ ^1P^o$ (squares) states in Fig. 5(b) as a function of time. Rabi oscillations take place between them.

Finally, we show in Figs. 6(a)-6(d) the PADs at the photoelectron energies corresponding to the first four ATI peaks (see Fig. 4) by the LP pulse at the peak intensity of $I = 5 \times 10^{11}$ W/cm². Different ATI peaks exhibit different PADs, since different partial waves make different contributions with different total phase shifts. This is the reason why the PADs in Figs. 6(a) and 6(c) and also Figs. 6(b) and 6(d) resemble each other, since the accessible continua belong to the same parity. We now have a closer look at Fig. 6(a). The PAD has a typical profile for two-photon ionization from an initial S state with one secondary maximum at $\theta = 90^\circ$ and two minima at $\theta = 54^\circ$ and 126° , respectively. Similarly the PAD shown in Fig. 6(b) has a typical profile for three-photon ionization from an initial S state which exhibits two secondary maxima and three minima. Figures 6(c) and 6(d) present the PADs at the third and fourth ATI peaks shown in Fig. 4.

B. Ionization by the third harmonic of a Ti:sapphire laser

In this subsection we study two-photon ionization by the third harmonic of the Ti:sapphire laser at the photon energy of 4.65 eV, which is schematically shown in Fig. 7. Although the detuning from the $4s5p\ ^1P^o$ bound state is only 0.1 eV which is even smaller than the case of the second harmonic in the previous subsection, we do not expect any important enhancement in the ionization process because the dipole moment for the transition $4s^2\ ^1S^e \rightarrow 4s5p\ ^1P^o$ is much smaller than that for the $4s^2\ ^1S^e \rightarrow 4s4p\ ^1P^o$ (see Table II). Actually the OSs for the $4s^2\ ^1S^e \rightarrow 4s5p\ ^1P^o$ transition is anomalously small. This is in contrast with the more regular decrease of OSs for the $3s^2\ ^1S^e \rightarrow 3snp\ ^1P^o$ ($n = 3 - 6$) transitions of Mg [16].

First, we present the ionization yield in Fig. 8(a) as a function of peak intensity for the LP (solid) and CP (dashed) laser pulses. The curves for the LP and CP laser pulses look almost the same with a slope of 1.98 at the peak intensities lower than $I = 2 \times 10^{13}$ W/cm², which agrees very well with the LOPT prediction. This implies that the near-resonance with $4s5p\ ^1P^o$ makes very little contribution to the ionization yield. In Fig. 8(b) the ratio

between the ionization yield for CP and LP laser pulses, Y_{CP}/Y_{LP} , is shown as a function of peak intensity. We can see that the ionization yield by the LP and CP laser pulses are almost equal below the saturation intensity.

Figure 9 shows the PES by the LP (solid) and CP (dashed) laser pulses at the peak intensity of $I = 10^{13}$ W/cm². Note the large difference of the peak intensities we have employed for Figs. 4 and 9, which, however, results in the similar amount of the ionization yields. Interestingly, the PES exhibits more substructures around each ATI peak, labeled as (a)-(d) in Fig. 9, where substructure (b) is hard to recognize due to the overlap with the ATI peak. The substructures are equidistantly separated by the photon energy of 4.65 eV and appear for both LP and CP pulses. These substructures in the PES resemble those we have seen for Mg at $\omega = 4.65$ eV [4]. The fact that the substructures appear for both LP and CP pulses implies that the certain bound states accessible in both laser polarization could be responsible for them. The procedure we have employed to identify the origin of the substructures is very similar to that we have used for Mg in our previous paper [4]. By inspection we expect that the bound states $4snp\ ^1P^o$ ($n=4,5$, and 6) and $3d4p\ ^1P^o$ could generate such substructures. Since we propagate the TDSE on the atomic basis, we can easily check this speculation by solving the TDSE by artificially removing the particular state under suspect, and comparing the PES with the original one obtained by the complete atomic basis. In Figs. 10(a)-10(d) we show the comparisons of the PES calculated under the same laser parameters with those for Fig. 9. We show the results obtained after the removal of a particular bound state (dashed lines), namely (a) $4s4p\ ^1P^o$, (b) $4s5p\ ^1P^o$, (c) $4s6p\ ^1P^o$, and (d) $3d4p\ ^1P^o$ upon solving the TDSE, in comparison with the PES for the complete calculation (solid lines) with the complete atomic basis. When the $4s4p\ ^1P^o$ state is removed [Fig. 10(a)], the substructures on the left-side of each main peak are reduced or disappear, as highlighted by the circles. Similarly, by removing the $4s6p\ ^1P^o$ and $3d4p\ ^1P^o$ states in Figs. 10(c) and 10(d), another small spikes labeled as (c) and (d) in Fig. 9 disappear. As for Fig. 10(b) by artificially removing the *near-resonant* state $4s5p\ ^1P^o$, the height of the main ATI peaks is only slightly reduced since the state $4s5p\ ^1P^o$ brings a small contribution in the ionization process (see Table II). These comparisons indicate that the physical origin of the substructures labeled as (a)-(d) in Fig. 9 is quite similar to that we have already found for the singlet as well triplet states of Mg [4, 5]. Briefly, the *off-resonant* bound states such as $4s4p\ ^1P^o$, $4s6p\ ^1P^o$, and $3d4p\ ^1P^o$ and the *near-resonant* bound state

$4s5p\ ^1P^o$ are the origin of the substructures.

Finally, we show in Figs. 11(a)-11(d) the PADs for the first four ATI peaks in Fig. 9 by the LP pulse at the peak intensity of $I = 10^{12}$ W/cm². The peak intensity is chosen to be low to avoid any undesired complications at higher intensities. Again, different ATI peaks result in the different PADs. In order to examine the influence of the intermediate bound states with the $^1P^o$ symmetry on the PAD we make a comparison of PADs by artificially removing the $4s4p\ ^1P^o$ (dashed), $4s5p\ ^1P^o$ (dot-dashed), $4s6p\ ^1P^o$ (dot-dot-dashed), and $3d4p\ ^1P^o$ (dot-dotted) states. The results are shown in Fig. 12. It turns out that the PAD is very sensitive to the removal of the *off-resonant* $4s4p\ ^1P^o$ state (see Fig. 7), while the change is very little when other bound states, including the near-resonant $4s5p\ ^1P^o$ state, are removed.

V. CONCLUSIONS

We have theoretically studied multiphoton ionization of Ca by linearly and circularly polarized fs laser pulses at the photon energies of 3.1 eV and 4.65 eV in terms of the ionization yields, photoelectron energy spectra, and photoelectron angular distributions. At the photon energy of $\omega = 3.1$ eV, the ionization process is strongly enhanced due to the presence of the near-resonant $4s4p\ ^1P^o$ state which has a large dipole moment from the ground state, and the ionization yield is about four orders of magnitude larger compared with a case without a resonance. The photoelectron energy spectrum hardly shows substructures, because any possible substructures are buried between the strongly enhanced ATI peaks. In contrast, at the photon energy of $\omega = 4.65$ eV, the photoelectron energy spectrum exhibits many substructures due to the real excitation of the *near-resonant* $4s5p\ ^1P^o$ state and some *off-resonant* bound states such as $4s4p\ ^1P^o$, $4s6p\ ^1P^o$, and $3d4p\ ^1P^o$, ... etc. Interestingly, the far off-resonant $4s4p\ ^1P^o$ state still makes a very large contribution to the ionization processes in this case, which can be most clearly understood in terms of the photoelectron angular distribution.

Acknowledgments

G.B. acknowledges hospitality from the Institute of Advanced Energy, Kyoto University during her stay. The work by G.B. and T.N. was respectively supported by a research program from the LAPLAS 3 and CNCSIS contract No. 558/2009 and a Grant-in-Aid for scientific research from the Ministry of Education and Science of Japan.

-
- [1] P. Agostini, F. Fabre, G. Mainfray, G. Petite, and N. K. Rahman, Phys. Rev. Lett. **42**, 1127 (1979).
 - [2] K. Burnett, V. C. Reed, and P. L. Knight, J. Phys. B **26**, 561 (1993).
 - [3] L. F. DiMauro and P. Agostini, Adv. At. Mol. Opt. Phys. **35**, 79 (1995).
 - [4] T. Nakajima and G. Buica, Phys. Rev. A **74**, 023411 (2006).
 - [5] G. Buica and T. Nakajima, Phys. Rev. A **79**, 013419 (2009).
 - [6] C. Froese Fischer and J. E. Hansen, Phys. Rev. A **24**, 631 (1981); J. Phys. B **18**, 4031 (1985).
 - [7] J. Mitroy, J. Phys. B **26**, 3703 (1993).
 - [8] M. Aymar, C. H. Greene, and E. Luc-Koenig, Rev. Mod. Phys. **68**, 1015 (1996).
 - [9] J. E. Hansen, C. Laughlin, H. W. van der Hart, and G. Verboekhaven, J. Phys. B **32**, 2099 (1999).
 - [10] C. F. Fischer and G. Tachiev, Phys. Rev. A **68**, 012507 (2003).
 - [11] S. Benec'h and H. Bachau, J. Phys. B **37**, 3521 (2004).
 - [12] L. F. DiMauro, Dalwoo Kim, M. W. Courtney, and M. Anselment, Phys. Rev. A **38**, 2338 (1988).
 - [13] Y.-L. Shao, V. Zafiropoulos, A. P. Georgiadis, and C. Fotakis, Z. Phys. D **21**, 299 (1991).
 - [14] S. Cohen, I. Lontos, A. Bolovinos, A. Lyras, S. Benec'h and H. Bachau, J. Phys. B **39**, 2693 (2006).
 - [15] L. A. A. Nikolopoulos, G. Buica-Zloh, and P. Lambropoulos, Eur. Phys. J. D **26**, 245 (2003).
 - [16] G. Buica and T. Nakajima, J. Quant. Spectrosc. Rad. Transf. **109**, 107 (2008).
 - [17] P. Lambropoulos, P. Maragakis, and J. Zhang, Phys. Rep. **305**, 203 (1998).
 - [18] H. Bachau, E. Cormier, P. Decleva, J. E. Hansen, and F. Martin, Rep. Prog. Phys. **64**, 1601 (2001).
 - [19] T. N. Chang *Many-body theory of Atomic Structure and Photoionization*, (World Scientific, Singapore, 1993), p. 213.
 - [20] X. Tang, T. N. Chang, P. Lambropoulos, S. Fournier, and L. F. DiMauro, Phys. Rev. A **41**, 5265 (1990).
 - [21] T. N. Chang and X. Tang, Phys. Rev. A **46**, R2209 (1992).
 - [22] M. W. J. Bromley and J. Mitroy, Phys. Rev. A **65**, 062505-1 (2002).

- [23] NIST Atomic Spectra Database, <http://physics.nist.gov/>.
- [24] H. J. Werner and W. Meyer, Phys. Rev. A **14**, 915 (1976).
- [25] R. Moccia and P. Spizzo, J. Phys. B **21**, 1133 (1987); **21**, 1121 (1988); **21**, 1145 (1988); S. Mengali and R. Moccia, *ibid.* **29**, 1597 (1996).
- [26] T. N. Chang and X. Tang, Phys. Rev. A **44**, 232 (1991).
- [27] A. Burgess, Proc. Phys. Soc. **81**, 442 (1963).
- [28] W. H. Parkinson, E. M. Reeves, and F. S. Tomkins, J. Phys. B **9**, 157 (1976).
- [29] G. Smith, J. Phys. B **21**, 2827 (1988).
- [30] G. Smith and D. St. J. Raggett, J. Phys. B **14**, 4015 (1981).
- [31] L. P. Lellouch and L. R. Hunter, Phys. Rev. A **36**, 3490 (1987).
- [32] Y. Gontier and M. Trahin, Phys. Rev. A **7**, 2069 (1973).
- [33] P. Lambropoulos, Phys. Rev. Lett. **28**, 585 (1972).
- [34] H. R. Reiss, Phys. Rev. Lett. **29**, 1129 (1972).
- [35] S. Klarsfeld and A. Maquet, Phys. Rev. Lett. **29**, 79 (1972).

Table I. Comparison of the energies for the first ionization threshold and the first few low-lying states of Ca. The energies are expressed in eV with respect to the energy of Ca^{2+} .

	Present	Theory [7]	Theory [9]	NIST [23]
$E_{\text{Ca}^+(4s)}$	-11.87199	-11.87112	-11.87179	-11.87172
$E_{4s^2\ ^1S^e}$	-18.011	-17.950	-17.988	-17.98488
$E_{4s5s\ ^1S^e}$	-13.859	-13.842	-13.857	-13.85406
$E_{4s6s\ ^1S^e}$	-12.973	-12.920	-12.950	-12.93991
$E_{4p^2\ ^1S^e}$	-12.796	-12.739	-12.793	-12.80404
$E_{4s4p\ ^1P^o}$	-15.065	-15.063	-15.071	-15.05236
$E_{4s5p\ ^1P^o}$	-13.427	-13.429	-13.436	-13.43073
$E_{4s6p\ ^1P^o}$	-12.798	-12.805	-12.821	-12.81733
$E_{3d4p\ ^1P^o}$	-12.512	-12.522	-12.543	-12.53782
$E_{4s3d\ ^1D^e}$	-15.217	-15.230	-15.286	-15.27586
$E_{4s4d\ ^1D^e}$	-13.321	-13.322	-13.377	-13.36048
$E_{4p^2\ ^1D^e}$	-12.901	-12.914	-12.939	-12.93626
$E_{4s5d\ ^1D^e}$	-12.658	-12.650	-12.666	-12.66359
$E_{3d4p\ ^1F^o}$	-12.925	-12.934	-12.964	-12.95882
$E_{4s4f\ ^1F^o}$	-12.728	-12.723	-12.737	-12.73494
$E_{4s5f\ ^1F^o}$	-12.428	-12.424	-12.430	-12.42978
$E_{4s6f\ ^1F^o}$	-12.258	-12.255	-12.259	-12.25899

Table II. Comparison of the absorption oscillator strengths (in atomic units and length/velocity gauge) between the few representative bound states with $^1S^e$, $^1P^o$, $^1D^e$, and $^1F^o$ symmetries.

$4s^2\ ^1S^e \rightarrow$	$4s4p\ ^1P^o$	$4s5p\ ^1P^o$	$4s6p\ ^1P^o$	$3d4p\ ^1P^o$
Present	1.921/1.756	4.115/3.563[−3]	2.677/2.151[−2]	7.496/5.056[−2]
Theory [7]	1.82/1.781	1.08/2.30[−3]	3.72/3.14[−2]	7.27/6.66[−2]
Theory [9]	1.745	1.95[−3]	3.62[−2]	6.46[−2]
NIST [23]	1.75		4.32[−2]	7.01[−2]
Experimental [28]	1.75	9.0[−4]	4.1[−2]	6.6[−2]
$4s4p\ ^1P^o \rightarrow$	$4s5s\ ^1S^e$	$4s6s\ ^1S^e$	$4p^2\ ^1S^e$	$4s7s\ ^1S^e$
Present	0.112/0.091	2.189/3.536[−2]	0.110/0.129	1.648/1.655[−2]
Theory [7]	0.118/0.114	0.909/2.26[−2]	0.120/0.148	
Theory [9]	0.128	7.50[−3]	0.116	1.01[−2]
Experimental [29]		9.0[−3]	0.114	1.33[−2]
$4s4p\ ^1P^o \rightarrow$	$4s4d\ ^1D^e$	$4p^2\ ^1D^e$	$4s5d\ ^1D^e$	$4s6d\ ^1D^e$
Present	0.229/0.198	0.573/0.604	0.299/0.298	5.768/5.814[−2]
Theory [7]	0.193/0.164	0.550/0.531	0.283/0.293	5.28/5.38[−2]
Theory[9]	0.206	0.548	0.265	4.527[−2]
Experimental [29]	0.207	0.58	0.28	4.4[−2]
$4s3d\ ^1D^e \rightarrow$	$4s4p\ ^1P^o$	$4s5p\ ^1P^o$	$4s6p\ ^1P^o$	$3d4p\ ^1P^o$
Present	1.14[−3]/5.936[−2]	5.730/7.876[−2]	6.112/6.756[−2]	5.378/5.171[−2]
Theory [7]	8.759[−4]/6.332[−2]	5.503/7.619[−2]	5.533/6.179[−2]	5.26/5.73[−2]
Theory [9]	1.46[−3]	5.85[−2]	6.568[−2]	5.166[−2]
NIST [23]		4.9[−2]	7.5[−2]	7.6[−2]
Experimental [30, 31]	1.02[−3]	5.985[−2]	5.66[−2]	6.76[−2]
$4s3d\ ^1D^e \rightarrow$	$3d4p\ ^1F^o$	$4s4f\ ^1F^o$	$4s5f\ ^1F^o$	$4s6f\ ^1F^o$
Present	6.877/3.397[−2]	0.140/0.117	5.657/5.161[−2]	3.053/2.842[−2]
Theory[7]	9.25/5.45[−2]	0.129/0.111	4.99/4.56[−2]	2.23/2.27[−2]
Theory[9]	7.144[−2]	0.131	5.57[−2]	3.038[−2]
NIST [23]	9.8[−2]	9.39[−2]	7.6[−2]	3.2[−2]
Experimental [30]	9.8[−2]	0.138		

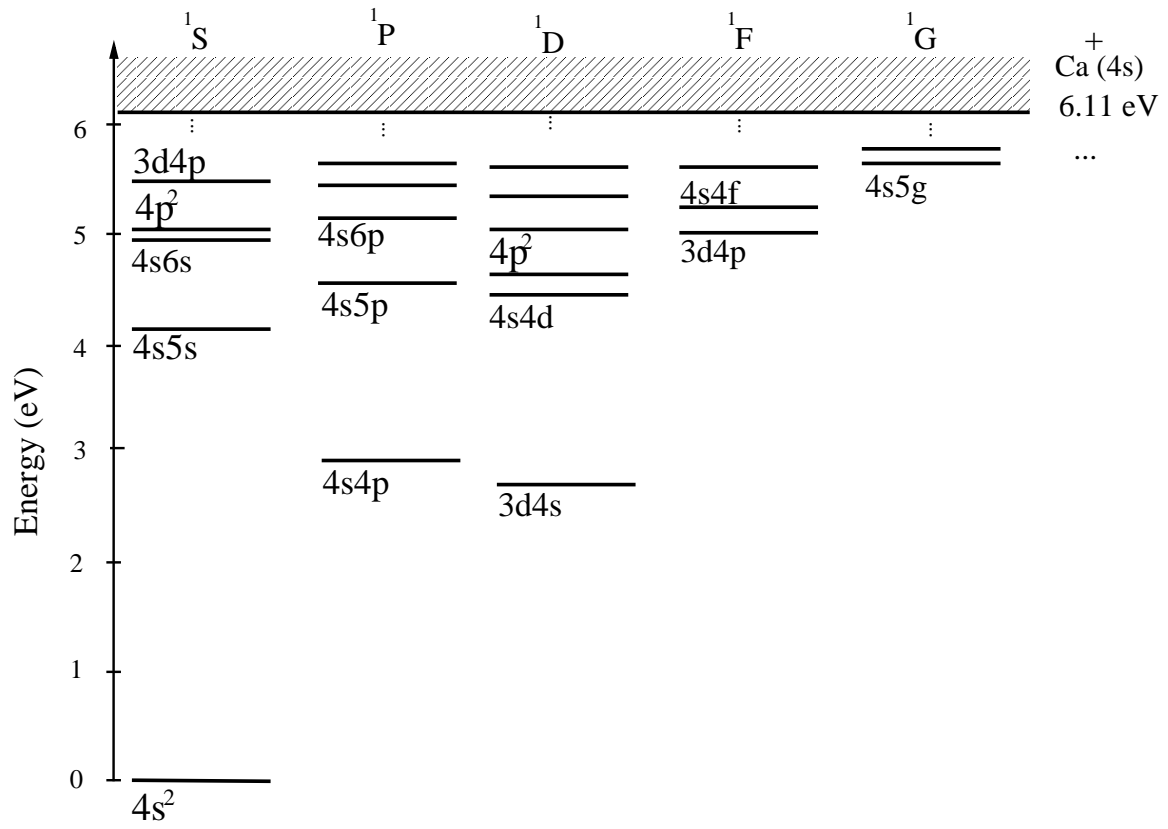


FIG. 1: Relevant energy levels of Ca.

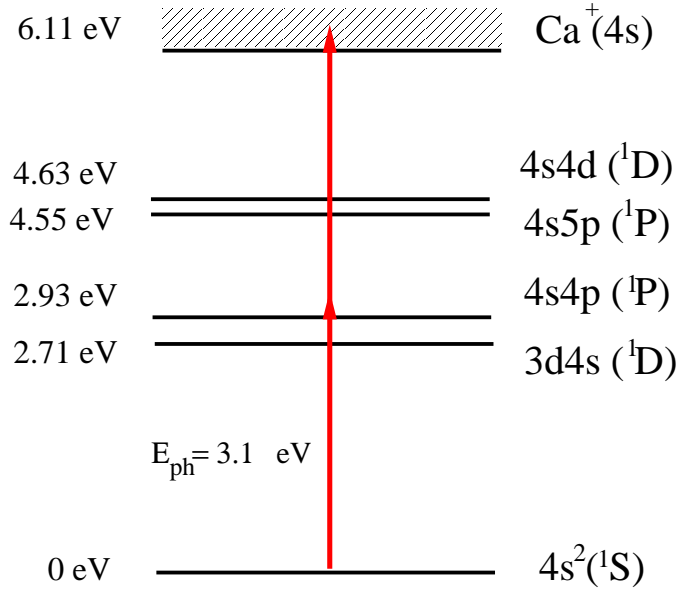


FIG. 2: Relevant energy levels for ionization at the photon energy of 3.1 eV. The energy detuning from the $4s4p ^1P^o$ bound state is 0.17 eV.

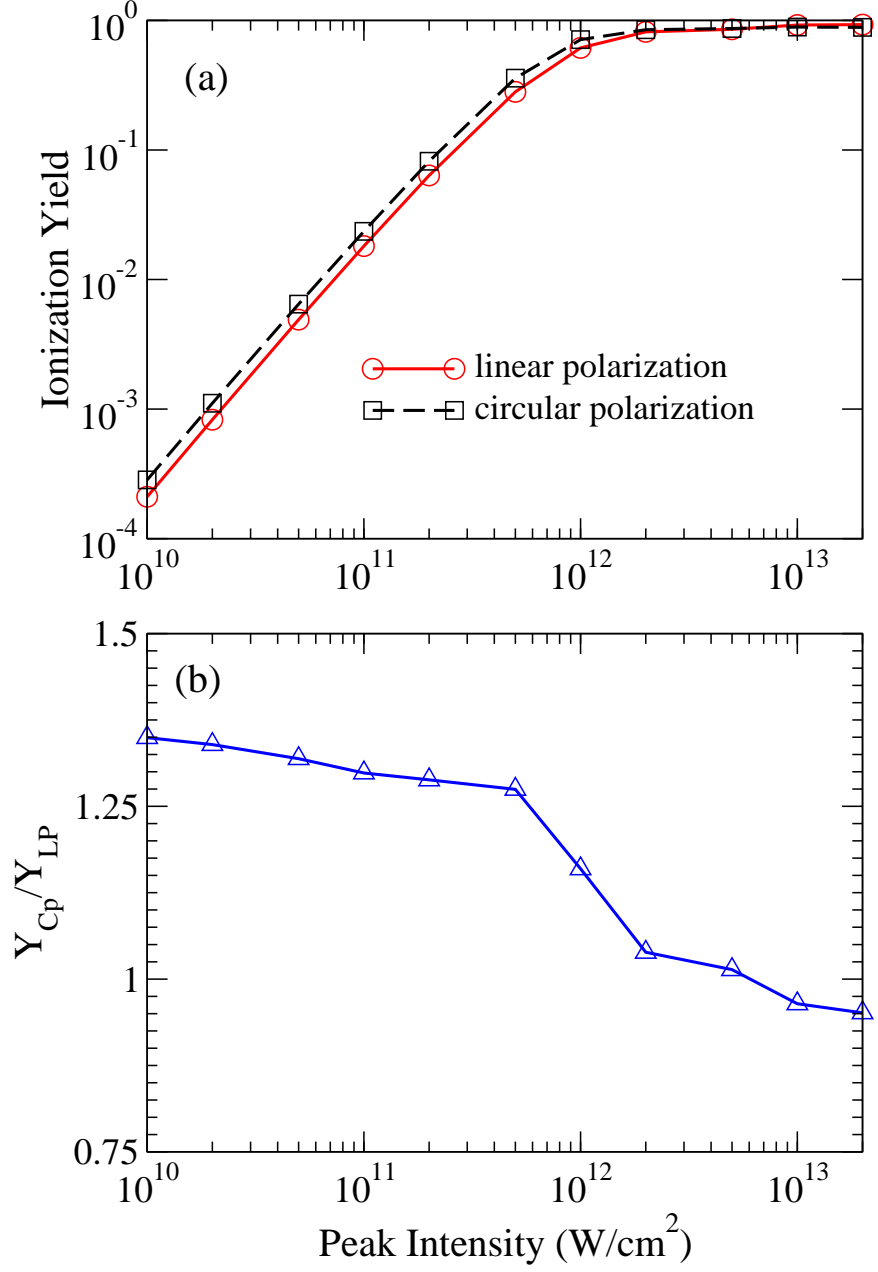


FIG. 3: (Color Online) (a) Ionization yield as a function of peak intensity by the linearly (solid) and circularly polarized (dashed) laser pulses at the photon energy of 3.1 eV. (b) Ratio of the ionization yield by the circularly polarized laser pulse, Y_{CP} , to that by the linearly polarized laser pulse, Y_{LP} .

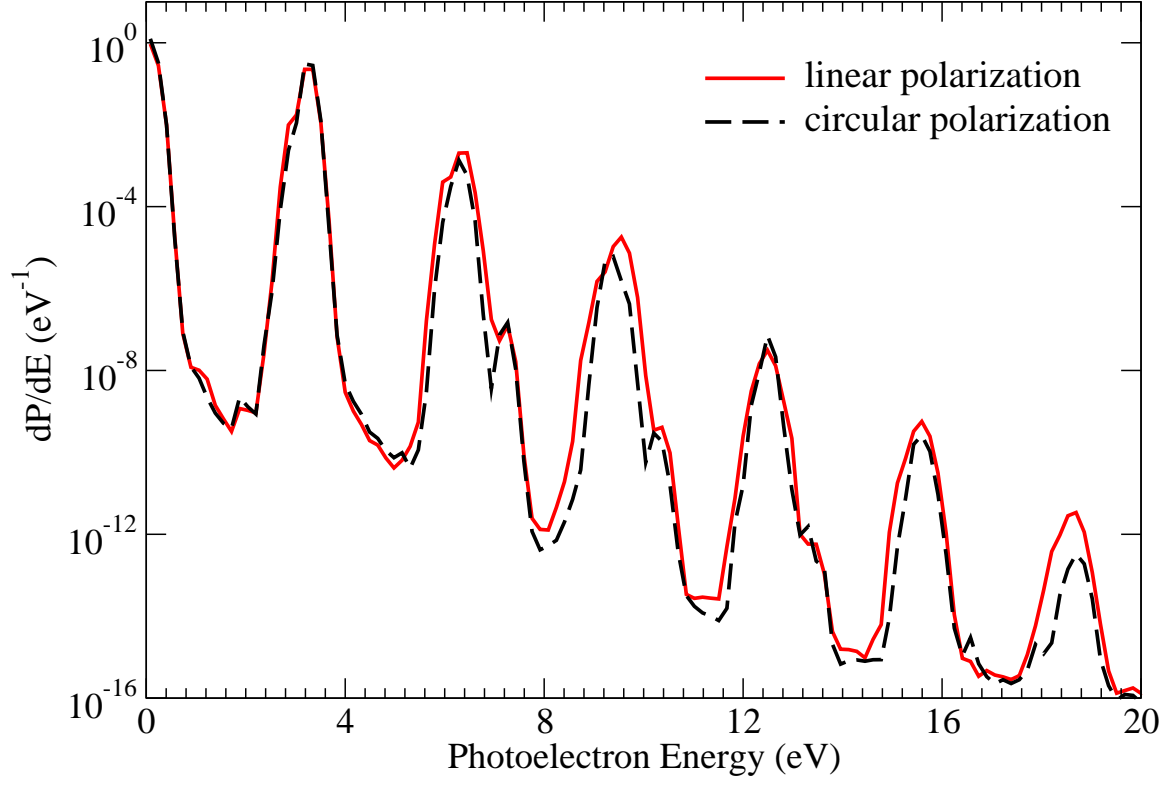


FIG. 4: (Color Online) Photoelectron energy spectra by the linearly (solid) and circularly polarized (dashed) laser pulses at the photon energy of 3.1 eV and the peak intensity of $5 \times 10^{11} \text{ W/cm}^2$.

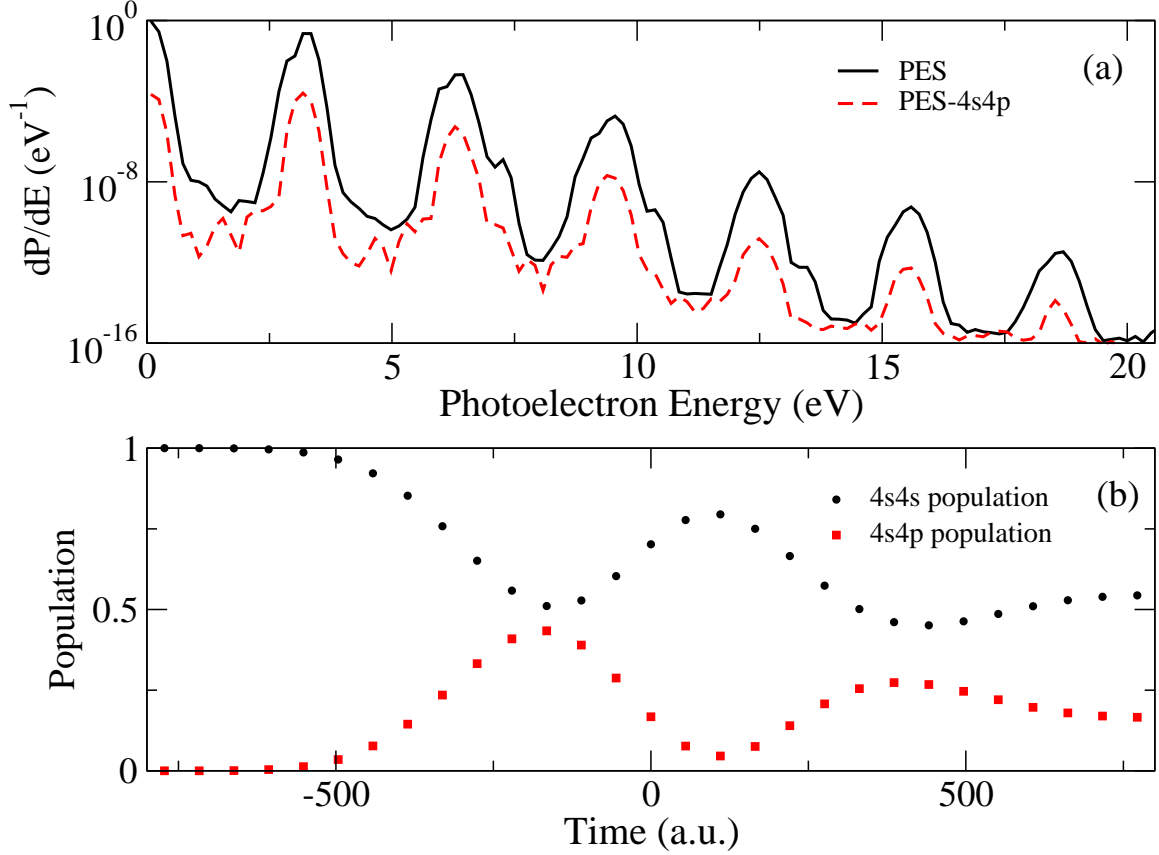


FIG. 5: (Color Online) (a) Comparison of the photoelectron energy spectra at the photon energy of 3.1 eV. Solid line represents the result obtained from the complete atomic basis, while the dashed line represents the result from the atomic basis without the $4s4p\ ^1P^o$ state when solving the time-dependent Schrödinger equation. (b) Comparison of the populations of the $4s^2\ ^1S^e$ (circles) and $4s4p\ ^1P^o$ (squares) states as a function of time. The laser pulse is linearly polarized and the peak intensity is 5×10^{11} W/cm².

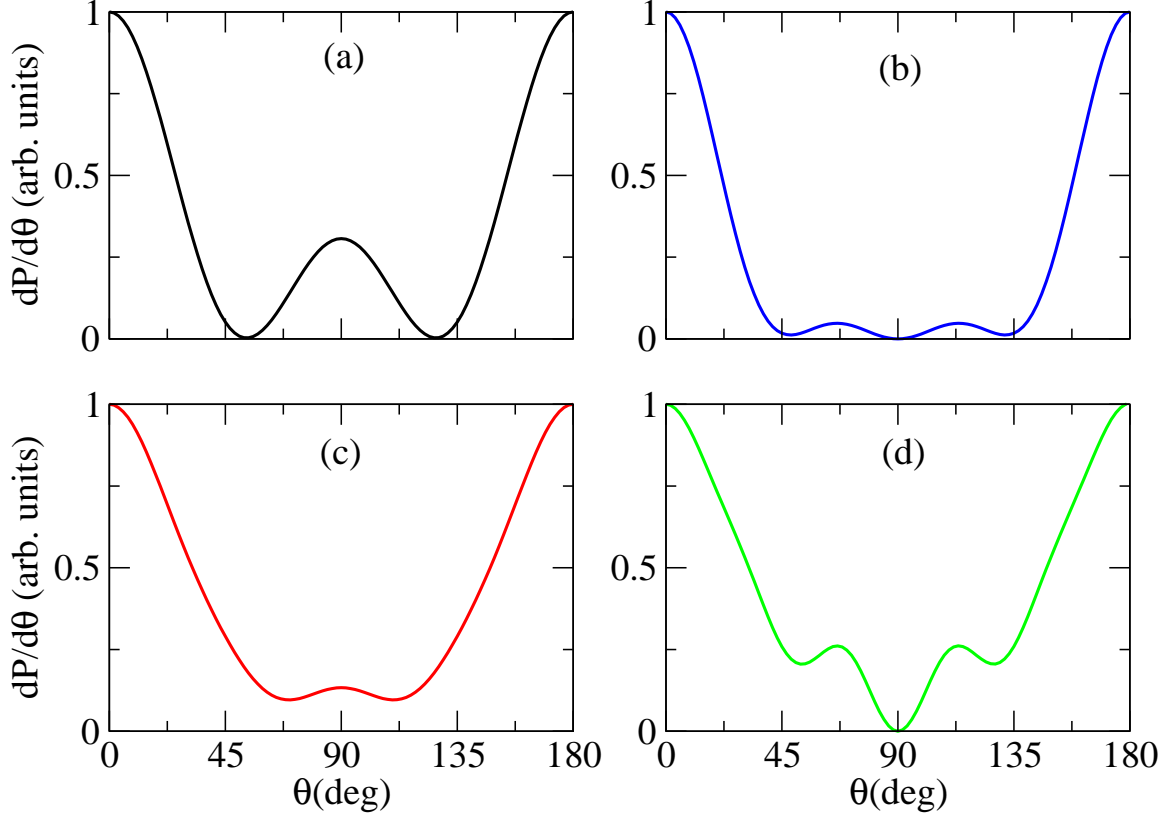


FIG. 6: (Color Online) Photoelectron angular distributions at the photon energy of 3.1 eV, corresponding to the (a) first, (b) second, (c) third, and (d) fourth ATI peaks in Fig. 4. The laser pulse is linearly polarized and the peak intensity is 5×10^{11} W/cm².

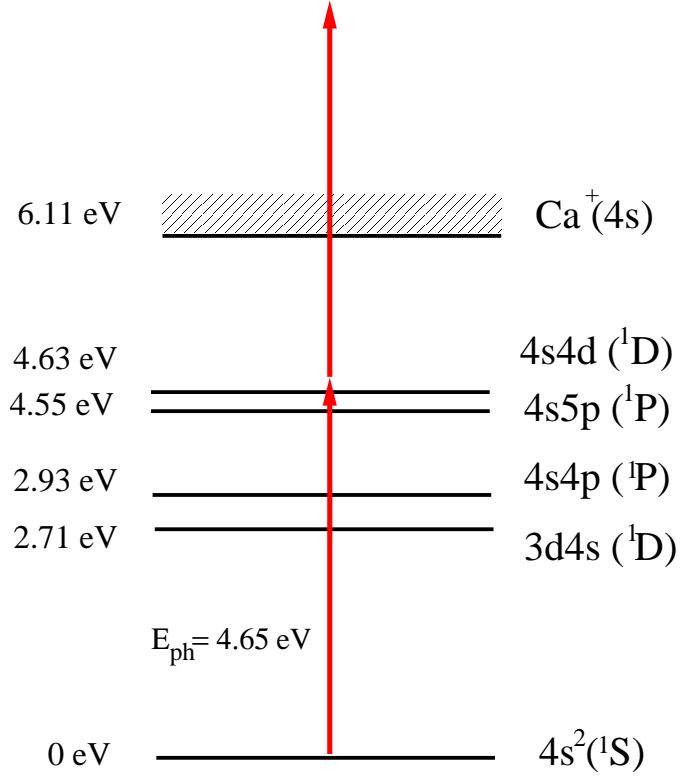


FIG. 7: Relevant energy levels for ionization at the photon energy of 4.65 eV. The energy detuning from the $4s5p\ ^1P^o$ bound state is 0.1 eV.

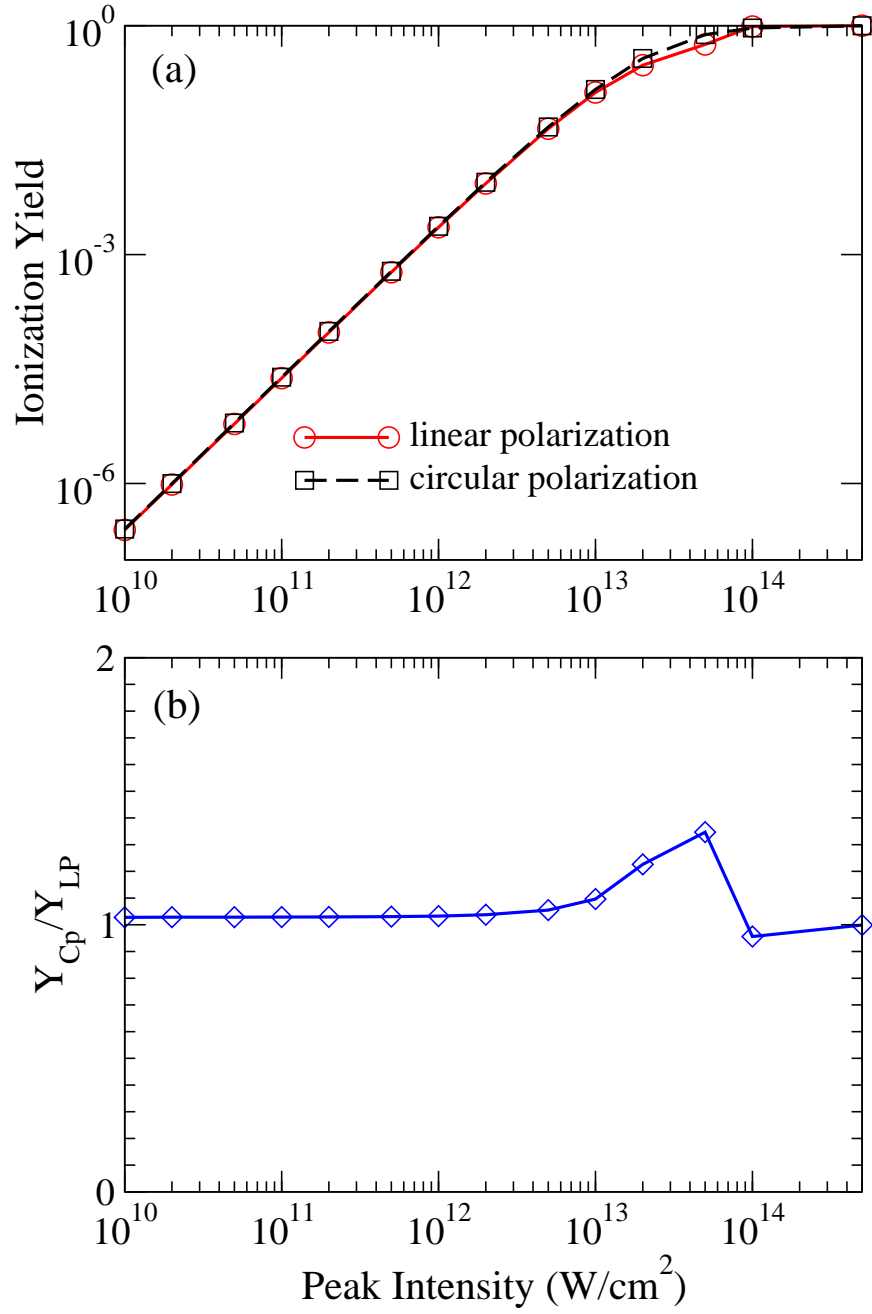


FIG. 8: (Color Online) (a) Ionization yield as a function of peak intensity by the linearly (solid) and circularly (dashed) polarized laser pulses at the photon energy of 4.65 eV. (b) Ratio of the ionization yield by the circularly polarized laser pulse, Y_{CP} , to that by the linearly polarized laser pulse, Y_{LP} .

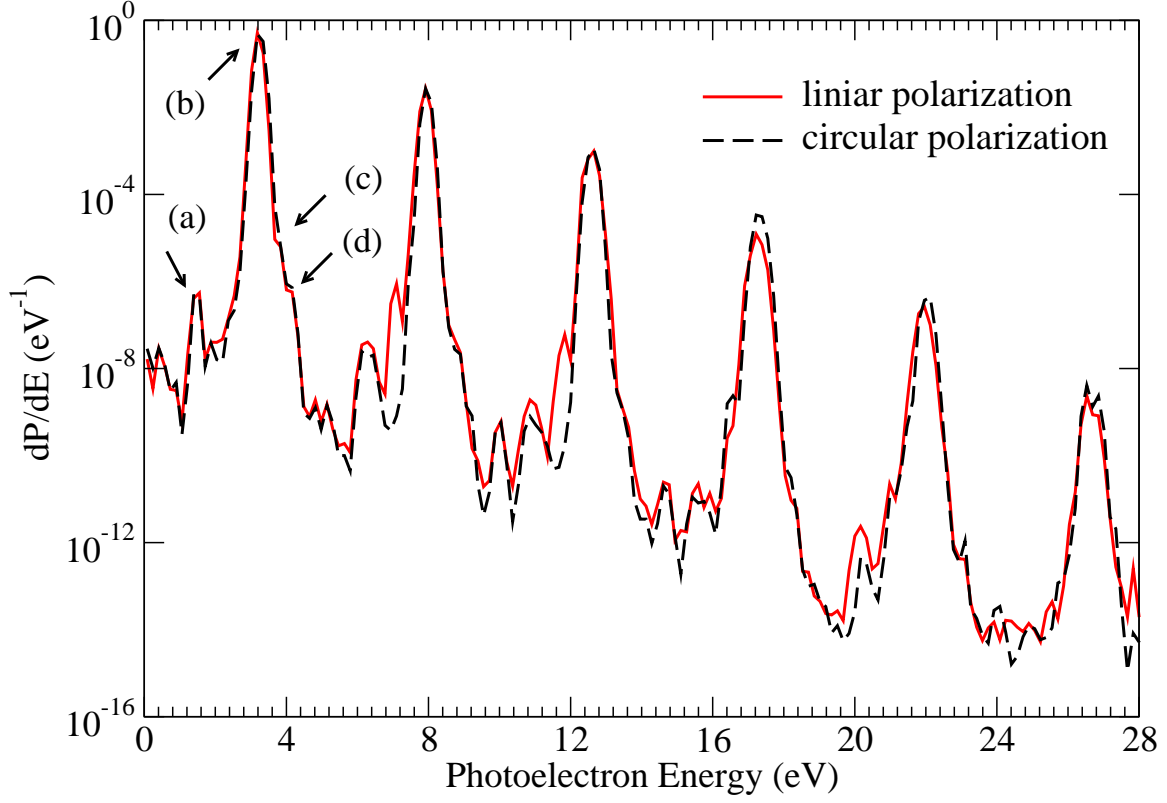


FIG. 9: (Color Online) Photoelectron energy spectra by the linearly (solid) and circularly polarized (dashed) laser pulses at the photon energy of 4.65 eV and the peak intensity of 10^{13} W/cm². (a)-(d) represent the substructures.

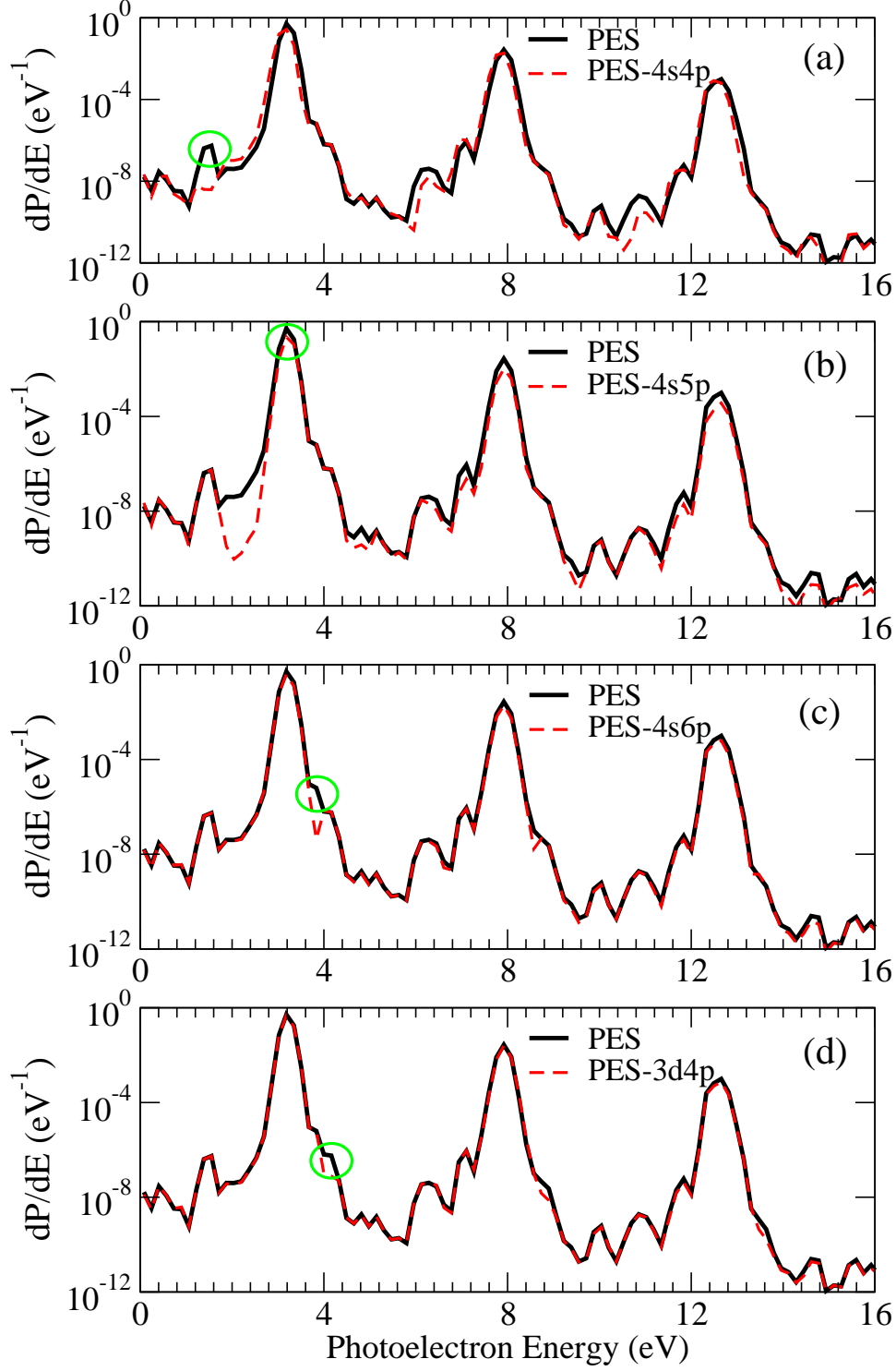


FIG. 10: (Color online) Comparison of the photoelectron spectra at the photon energy of 4.65 eV when the (a) $4s4p\ ^1P^o$, (b) $4s5p\ ^1P^o$, (c) $4s6p\ ^1P^o$, and (d) $3d4p\ ^1P^o$ states are artificially removed from the atomic basis when solving the time-dependent Schrödinger equation. The laser pulse is linearly polarized and the peak intensity is 10^{13} W/cm^2 .

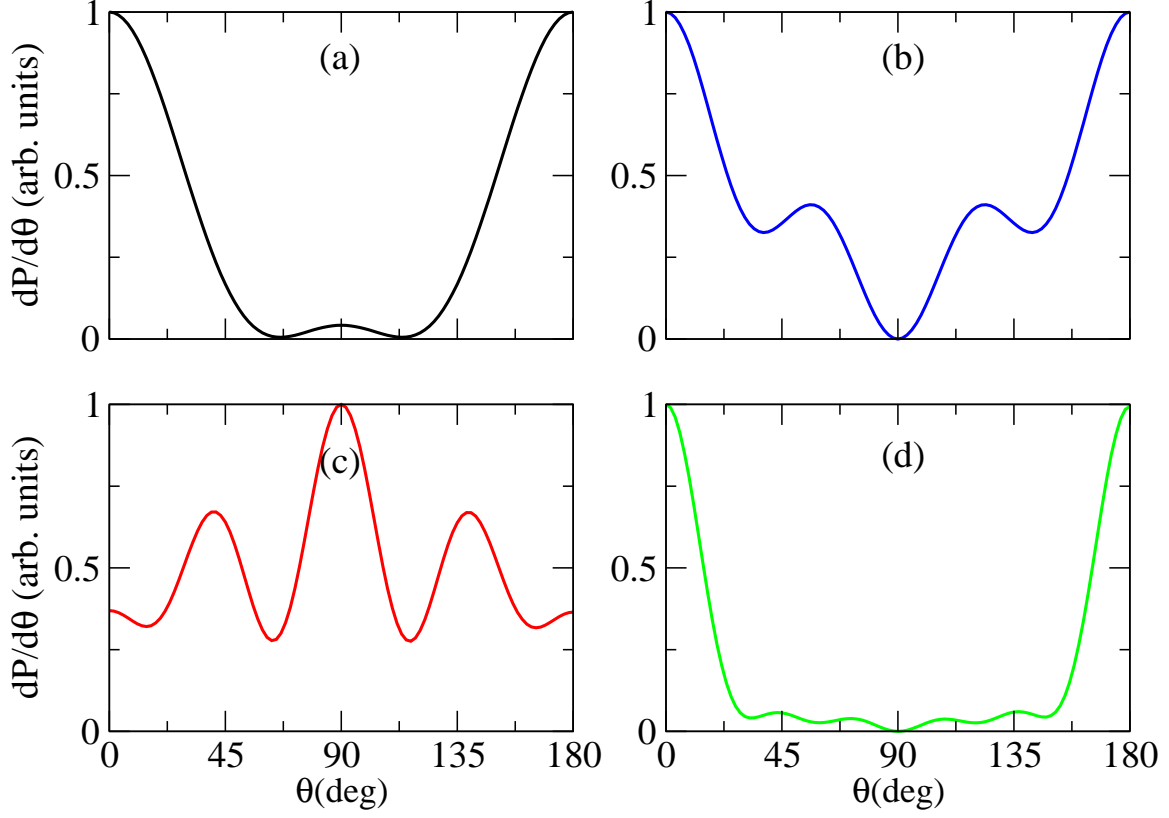


FIG. 11: (Color Online) Photoelectron angular distributions at the photon energy of 4.65 eV, corresponding to the (a) first, (b) second, (c) third, and (d) fourth ATI peaks in Fig. 9. The laser pulse is linearly polarized and the peak intensity is 10^{12} W/cm².

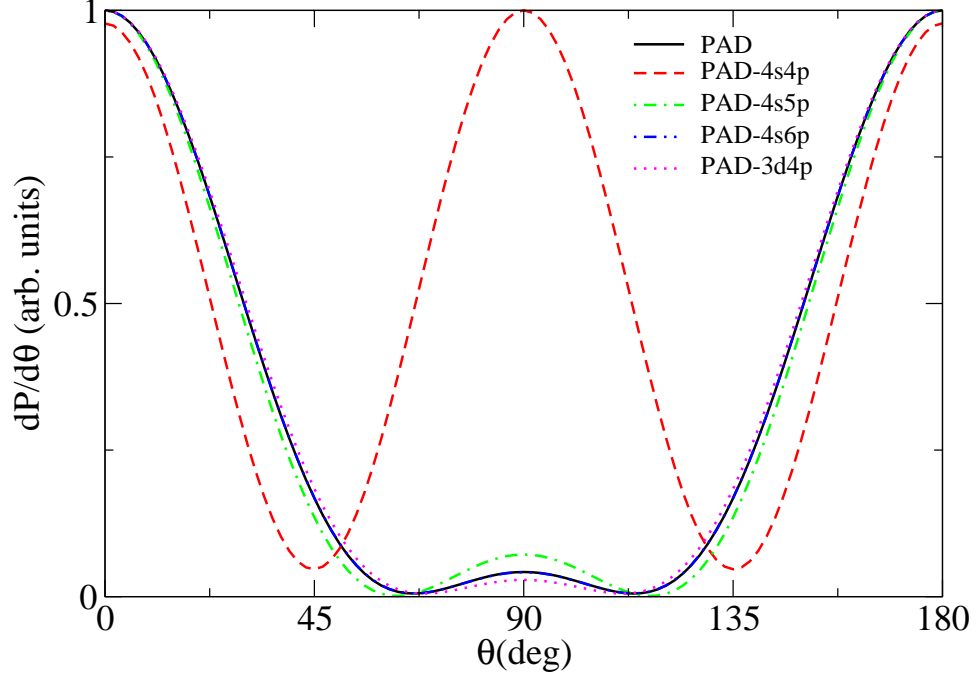


FIG. 12: (Color Online) Comparison of the photoelectron angular distributions by a linearly polarized laser pulse at the photon energy of 4.65 eV when the $4s4p\ ^1P^o$, $4s5p\ ^1P^o$, $4s6p\ ^1P^o$, and $3d4p\ ^1P^o$ bound states of Ca are artificially removed from the atomic basis when solving the time-dependent Schrödinger equation. The peak intensity is 10^{12} W/cm².